

Flowfield Structure in a Fin-Slot Solid Rocket Motor (Part I)

Jeffrey D. Moore,^{*} Robert B. Wehrman,[†] Kenneth K. Kuo,[‡] Peter J. Ferrara,[§] and Ryan W. Houim^{*}
Pennsylvania State University, University Park, Pennsylvania 16802

DOI: 10.2514/1.38164

To accurately predict the overall ignition transient for the reusable solid rocket motor of the space shuttle booster with head-end fin slots, it is necessary to acquire detailed flowfield structure and energy transfer rates on the exposed inert fin-slot propellant surfaces. This paper is the first of a two-part study and deals with the internal flowfield structure and heat-transfer characteristics in the fin-slot region. A subscale (1:10) pie-shaped fin-slot motor was designed to perform diagnostic measurements. An array of 36 flush-mounted heat-flux gauges was installed to detect the local temperature-rise rates at representative regions perpendicular to the propellant surface. Flowfield visualizations were conducted by applying either a chalk-powder/kerosene mixture or many small threads taped to various locations on the inner surface of the sacrificial window of the fin-slot region for high-speed video camera recording. Computational fluid dynamics simulations were performed for modeling the internal flowfield of the test rig. Results were used to develop a heat-transfer correlation governed by the internal flowfield structure within the fin-slot region. The theoretically calculated and experimentally observed internal flowfield patterns were similar in nature. The heat-transfer rates determined from the developed correlation matched the measured data trend within the experimental error. The flowfield structure and heat-transfer rate distribution are mainly governed by the major recirculating flow induced by the igniter jet.

Nomenclature

A	=	area
C	=	specific heat
C_f	=	skin friction coefficient
d	=	diameter
D_H	=	hydraulic diameter
H	=	height
h_c	=	convective heat-transfer coefficient
k_f	=	thermal conductivity
L	=	length
\dot{m}	=	mass flow rate
M_w	=	molecular weight
Nu	=	Nusselt number
P	=	pressure
Pr	=	Prandtl number
\dot{q}''	=	heat flux
R	=	gas constant
Re	=	Reynolds number
T	=	temperature
t	=	time
U	=	velocity
u	=	velocity in x direction
u_t	=	friction velocity
v	=	velocity in y direction
W	=	fin-slot thickness
x	=	x -spatial location on fin
y	=	y -spatial location on fin

β	=	angle of fin slot
γ	=	specific heat ratio
δ	=	thickness
η	=	wavelength function
λ	=	wavelength
μ	=	dynamic viscosity
ρ	=	density
σ	=	molecule hard sphere diameter
τ	=	shear stress
ν	=	kinematic viscosity

Subscripts

air	=	airflow
B	=	bulk
BDT	=	blow-down tunnel
Cu	=	copper
D_H	=	hydraulic diameter
FS	=	fin slot
gas	=	gas
ign	=	igniter
local	=	local
max	=	maximum
prop	=	live igniter propellant
res	=	resultant
surf	=	surface
th	=	throat
vel	=	velocity
w	=	wall

Presented as Paper 4772 at the 42nd AIAA/ASME/SAE/ASEE Joint Propulsion Conference and Exhibit, Sacramento, CA, 9–12 July 2006; received 20 April 2008; revision received 29 September 2008; accepted for publication 30 September 2008. Copyright © 2008 by Kenneth K. Kuo. Published by the American Institute of Aeronautics and Astronautics, Inc., with permission. Copies of this paper may be made for personal or internal use, on condition that the copier pay the \$10.00 per-copy fee to the Copyright Clearance Center, Inc., 222 Rosewood Drive, Danvers, MA 01923; include the code 0748-4658/09 \$10.00 in correspondence with the CCC.

^{*}Ph.D. Candidate, Department of Mechanical and Nuclear Engineering, 139 Research Building East. Student Member AIAA.

[†]Graduate Student, Department of Mechanical and Nuclear Engineering, 139 Research Building East. Student Member AIAA.

[‡]Distinguished Professor, Department of Mechanical and Nuclear Engineering, 140 Research Building East. Fellow AIAA.

[§]Research Assistant, Department of Mechanical and Nuclear Engineering, High Pressure Combustion Lab. Student Member AIAA.

I. Introduction

IN THE area of solid rocket propellants, numerous researchers have studied the flame-spreading processes, flowfield structures, and ignition transients using a variety of laboratory-scale motors [1–5]. Despite the abundant research, very little work on flowfield structure and heat-transfer rates have been conducted in more complex propellant grain geometries. Examples include rocket propellant grains with fin slots in solid rocket motors (with some recent computational [5,6] and experimental [7] work performed in the aft-end fin slots) and computational flame-spreading studies of head-end fin slots [8].

One important application for these complex grains can be directly seen in the space shuttle solid rocket booster (SRB) where the

head-end fin-slot region acts as one of the four booster segments [9]. A major reason behind the incorporation of fin slots in the space shuttle SRB design is the benefit of the large propellant burning surface area of the fin slots, which provides a high amount of thrust in a short amount of time, vital to the space shuttle liftoff [10–12]. The importance of propellant grains with fin slots can be summarized by their following advantages: 1) a large propellant burning surface area, 2) a nearly constant total burning surface area, leading to a nearly constant thrust during motor firing, 3) a larger area for igniter product gases to ignite the main propellant grain, 4) a greater igniter product gas expansion, minimizing hoop stress in the motor, and 5) a reduced erosive burning in the motor [7]. It can be seen from these advantages that the ability to accurately predict the internal flowfield for the flame-spreading process, and eventually the overall ignition transient, can help with the future design of these complex fin-slot rocket motors and capitalize on its many advantages.

A better understanding of the overall ignition transient is an important concern and requirement for efficient burning of a solid rocket motor [13,14]. It is the behavior of the igniter product hot gases and motor geometry that can have the most influential effect on overall ignition transient flame-spreading phenomena [3]. Therefore, in order to improve the overall understanding of the internal flowfield phenomena and heat-transfer effects in head-end propellant grains with fin slots, a series of simulated clean gas and live igniter experiments were conducted. The actual flame-spreading measurements were conducted and reported in Part II of this overall study [15]. The experiments conducted in this work, as well as Part II [15] for actual flame-spreading measurements, took place in a 1:10 scale reusable solid rocket motor (RSRM). The observed internal flowfield structure information was used in the development of a heat-transfer correlation inside the fin-slot region.

II. Motivation and Objectives

To predict the flame-spreading process and eventually determine the overall ignition transient in a head-end fin-slot motor, the first area investigated was the initial phase of the overall ignition process. This phase included the internal flowfield structure and eventual development of ignition at certain locations (or induction interval) followed by flame spreading [1,4,13,16]. It is in this initial phase that the igniter-gas-induced flowfield directly influences the mechanism or propagation of the ignition front and flame spreading, because the ignition delay and the flame-spreading pattern depend strongly on the energy transfer rates from the igniter product gases to the propellant surface [1,4,17]. By understanding the internal flowfield more accurately and determining the local heat-transfer rates, a correlation between the two can be developed, making predictions of the flame-spreading event easier in these complex grain designs.

Therefore, the overall objective for this study was to obtain a better understanding of the relationship between the internal flowfield structure and local heat-transfer rates in the simulated fin-slot segment. The specific tasks conducted for reaching the overall objective were to 1) modify an existing laboratory-scale motor capable of simulating the internal flowfield processes in the head-end fin-slot region, 2) use an existing blow-down wind tunnel system to supply clean air at elevated pressures and temperatures as the simulated gas flow through the igniter nozzle, 3) use live pyrogen igniters to study the process of igniter products entering the RSRM grains, 4) observe and measure the internal flowfield characteristics using several diagnostics techniques, and 5) analyze experimentally observed flowfield structure and CFD (computational fluid dynamics) simulated results to develop a heat-transfer correlation within the head-end fin-slot segment of the simulated RSRM.

III. Method of Approach

To fully understand the flow characteristics in the fin-slot region of the forward segment of the space shuttle RSRM, two different experimental approaches were used. The first was a cold and hot airflow, using compressed air from a blow-down wind tunnel. The second was an igniter testing series, using live pyrogen igniter propellant for the simulated space shuttle solid rocket booster.

IV. Experimental Design

The study of the flame-spreading processes in the space shuttle RSRM was approached by using an approximately 1:10 scaled RSRM test rig. The test rig previously designed and operated to study the flame-spreading processes in an aft-end fin-slot solid rocket motor [7] was modified for this work. The existing motor housed a single, pie-shaped propellant holder, which was able to have inert or live space shuttle RSRM propellant samples cast on both sides, acting as the fin-slot-region propellant. This pie-shape propellant holder represented one of the 11-point star-shaped fin slots of the actual RSRM (see Fig. 1), supplying these experiments with two fin-slot regions for diagnostic studies. An exploded view of the approximately 1:10 scale RSRM test rig is shown in Fig. 2.

The test rig consisted of eight major components, including the main chamber for housing the propellant holder, a fin-slot propellant holder, a sacrificial inner acrylic window, an outer main viewing acrylic window, an exit nozzle with bore section, an igniter body and nozzle, a diagnostic holder, and a coupling section to the blow-down wind tunnel. The coupling section was used for clean airflow experiments only. For experiments using live igniter cartridges, the coupling section to the blow-down tunnel was removed and replaced by a small pyrotechnic squib inserted into the igniter body [18].

A. Main RSRM Test Rig Design

For this series of test runs, the main chamber exit nozzle was graphite with a constant diameter of 5.33 cm. The reason behind this large diameter was to prevent any large pressurization levels in the chamber, because only the initial igniter flow effects were to be examined. The igniter nozzle throat was also graphite and the diameter was set at 0.56 cm for all the live igniter experiments. Both nozzles were examined after each test for erosion and replaced when needed. For the cold and hot airflow experiments, the igniter nozzle diameter and length were altered to compensate for a variety of upstream pressures and, more important, to ensure that the impinging angle and location in the fin-slot region were maintained. This is

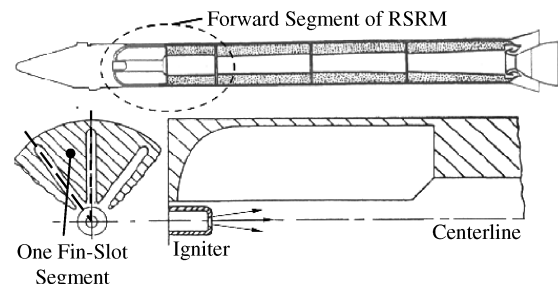


Fig. 1 Schematic of the RSRM forward segment fin-slot region [8].

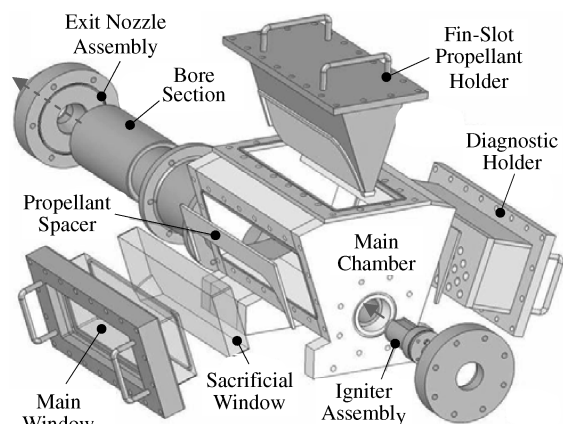


Fig. 2 Exploded view of the approximately one-tenth-scale RSRM test rig.

explained more in-depth in Sec. IV.C.1. Maintaining similarity to the actual RSRM, the igniter area expansion ratio was held at 1.83 and the expansion angle equaled 27 deg. Heat-transfer diagnostics, discussed in the next section, were applied on one side to the fin-slot motor. On the opposite side of the test rig, the inner window was 5.10-cm thick and was considered sacrificial, because it was in contact with the flow. Flow visualization diagnostics, which are also discussed in the next section, were applied to the inner surface of the sacrificial window during airflow testing. The main outer window was 10.2-cm thick and was able to be reused multiple times, because it did not come in contact with the flow. The windows were retained with a rectangle-shaped flange and gasket that bolted to the fin-slot motor simulator. The exit nozzle was installed at the rear end of the motor, along with an added center port section for increasing the overall internal volume and maintaining similarity with the actual head-end RSRM section. Lastly, the inert propellant had a constant web thickness of 0.5 cm; this thickness was sufficient enough to simulate the thermally thick propellant grain.

B. Diagnostic Methods

To directly measure the incoming hot product or hot airflow patterns in the head-end fin-slot region, 36 slug-type heat-flux gauges were designed and fabricated. A 25- μm *E*-type thermocouple was attached to a copper disk sensor, which acted as a thin layer of thermal energy storage material, shown in Fig. 3. The thermocouple was housed in a small, threaded steel housing. Zirconia ceramic material was coated around the copper disk to protect the internal wiring of the thermocouple from the intense fin-slot-region heat flux and to minimize the heat-transfer losses from the copper disk to the steel housing. The exposed copper surface was set at a diameter of 0.64 cm to ensure that each gauge had the same surface area. The gauges operated by employing a lumped parameter assumption between the thermocouple and the copper disk (Biot number $\ll 0.1$), which allowed the temperature–time trace to be instantaneously captured at different positions throughout the fin-slot region. These positions were divided into five rows, with seven or eight gauges per row. Each gauge was flush mounted onto a large diagnostic holder to prevent any cavities between the gauge and induced flow in the fin-slot region. The diagnostic holder (see Fig. 2) was then installed into the fin-slot motor directly across from the inert propellant surface, creating the aforementioned fin-slot region.

From the temperature–time profiles, the local heat flux at each position could be determined by the copper plate properties and analyzing the calculated dT/dt using the following equation:

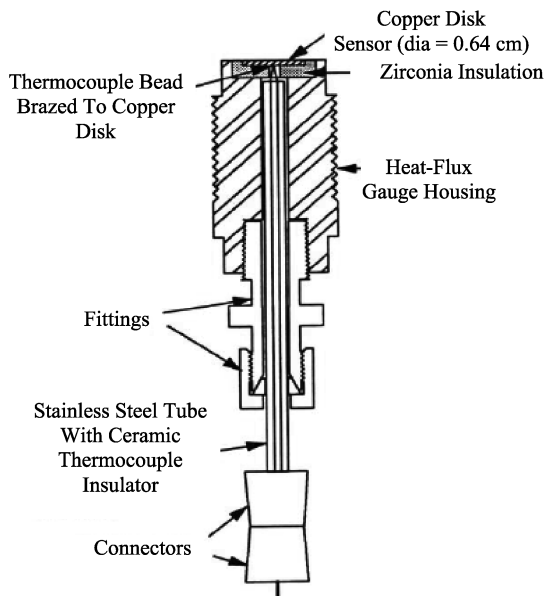


Fig. 3 Schematic drawing of the slug-type heat-flux gauge.

$$\dot{q}'' = \rho_{\text{Cu}} C_{\text{Cu}} \delta_{\text{Cu}} \left(\frac{dT}{dt} \right) \quad (1)$$

The specific heat was assumed to be constant due the small temperature change. Along with the heat-flux gauges, a digital high-speed camera was used to capture the live ignition event at 10,000 fps.

To observe the cold airflow patterns in the fin-slot region, two visualization methods were used. The first involved the utilization of a chalk powder and kerosene mixture. Twenty-five grams of blue-colored chalk were added to 50 mL of kerosene and mixed to form a paintlike substance. This mixture was spread out evenly by a spatula across the inner surface of the sacrificial window area exposed to the flow. The kerosene was then allowed to evaporate, leaving a thin layer of chalk powder on the inner window surface. Once the sacrificial window was exposed to the flow, the chalk powder would be swept along the inner surface and redistributed according to the surface flow pattern, providing the near-wall flowfield in the fin-slot region. The second flow visualization technique involved the use of fine threads taped at various locations on the inner surface of the sacrificial window. Once exposed to the flow, the threads were blown in different directions dictated by the fin-slot flowfield, which is governed by the simulated igniter nozzle geometry, simulated flow rate, and the fin-slot configuration. A high-speed camera was used to capture the flow characteristics observed by these two visualization methods.

C. Configuration of Compressed Airflow System

The simulation of clean airflow from the igniter nozzle into the fin-slot motor was accomplished by connecting the motor to a large blow-down wind tunnel, capable of flowing up to 9 kg/s of clean air. The blow-down tunnel air was supplied from two large air tanks (72 m³), containing compressed air up to pressures of 4.93 MPa. The blow-down tunnel contained 4–1000 W heaters surrounded by a cluster of copper tubes acting as a packed bed heater. The heater was capable of heating 3 kg/s of the air from 298 to 900 K for 3 s test runs, with a gas temperature drop of no more than 30 K. For this series of testing, cold airflow ($T = 298$ K) was used for flow visualization studies, with warmer airflow (up to 723 K) to monitor heat-transfer effects.

1. Determination of Airflow Rate, Reynolds Number Test Condition, and Nozzle Throat Size

An analysis was performed to determine the desirable simulator igniter nozzle throat geometry and corresponding air tank pressure level and temperature to accurately simulate the live firing of the igniter in the laboratory-scale simulator. This way, a comparison could be made between the live igniter and hot airflow. Also, with hot airflow, many more experiments could be conducted to measure the induced flowfield.

Using live igniter firing predictions, the mass flow rate of the igniter (\dot{m}_{ign}) was found to be equal to 0.159 kg/s. From this knowledge, the Reynolds number through the core flow section at the igniter exit (Re_D) could be calculated based on the following baseline dynamic viscosity equation [19] and Re_D equation [9]:

$$\mu = 26.69 \frac{(M_w T)^{1/2}}{\sigma^2} \quad (2)$$

$$Re_D = \frac{4\dot{m}_{\text{ign}}}{\pi \mu d_{\text{ign}}} \quad (3)$$

Using the live igniter propellant data, the equations yielded a $Re_{D,\text{prop}} \sim 3.2 \times 10^5$ through the simulator igniter exit. Based on these actual igniter flow calculations, the igniter nozzle throat area (A_{ign}) for the laboratory-scale experiments were determined using a selected blow-down wind tunnel pressure level (P_{BDT}), temperature (T_{BDT}), and the choked nozzle flow equations [20]. To achieve

different simulated hot gas temperature, the blow-down wind tunnel stagnation temperatures ranged from $T_{BDT} = 298\text{--}450\text{ K}$ while P_{BDT} ranged from 1.20–3.45 MPa. Multiple igniter nozzle sizes (0.61–1.11 cm) were used depending on P_{BDT} and T_{BDT} , with $Re_{D,air}$ on the same order of magnitude as $Re_{D,prop}$, within the same turbulent flow regime, which was required for hot gas flow and live igniter flow comparisons. In this way, a variety of igniter flow velocities exiting the igniter nozzle could be measured, providing more data to support the heat-transfer correlation development.

2. CFD Simulation

To predict the internal igniter-induced flowfield structure, a CFD simulation was performed. The internal geometry (Volume = 6000 cm³) of the approximately 1:10 laboratory-scale head-end fin-slot simulator motor was modeled. The computational domain consisted of 515,970 hexahedral cells in the fluid domain and 222,190 hexahedral cells in the solid propellant domain. In this numerical simulation, only the heating of inert propellant was considered. Because the interface between the inert propellant and the fluid domain is neither at a constant heat flux nor at a constant temperature during the transient heating event from the igniter, a solid domain for the inert propellant was coupled to the fluid domain. The thermal properties of the solid region were assumed to be those of the propellant.

The igniter inlet was treated as a mass flow inlet with constant mass flow rate, total temperature, and thermal properties throughout the calculation. The igniter mass flow rate corresponded to a fraction of the total igniter-discharge flow rate, because the calculation only simulates a small wedge of the whole fin-slot propellant segment. The nozzle outlet of the combined domain was set to ambient pressure.

Turbulence was modeled using the detached eddy simulation method (DES) [21], which is a hybrid large-eddy simulation/Reynolds-averaged Navier–Stokes technique. The near-wall regions were modeled with the Spalart–Allmaras model [22] with wall functions and core flow calculated using the large eddy simulation methodology. All of the advection operators were discretized using the second-order upwind scheme with the advection upstream splitting method [23,24] for calculating the fluxes at the cell faces. The transport equations were marched explicitly in time, with a constant CFL value of 0.75. The results of the computation are presented in a later section.

3. Heat-Transfer Correlation Development

The first step in developing a suitable heat-transfer correlation for the fin-slot region required the construction of a flowfield structure. This was achieved by examining the data obtained from the induced flow experiments and incorporating the angular injection jet action as the driving force for the recirculating flow. Boundary conditions were applied based upon the no-slip condition of the wall surfaces. Next, each position in the fin-slot region was analyzed individually. This was accomplished by developing suitable functional forms of the u -, v -, and w -velocity components in the flowfield, and assigning a number of coefficients in the functional form to simulate the relative size of these recirculation zones. It is believed that the w -velocity component is extremely small in magnitude in the fin-slot region in comparison with the u - and v -velocity components and assumed to be negligible, especially for the initial preheating period. From flow observations, it was determined that the fin slot had three distinct flow regions, as shown in Fig. 4. Step by step, each region was evaluated for the u - and v -velocity component in terms of the x and y direction. The z -direction variation of the bulk flow velocity component is considered to be extremely small, except near the wall surfaces.

Once all the velocity components were tested at each spatial position, the overall flowfield was determined. Each velocity component was entered into a code to sum all of the u - and v -velocity terms, effectively creating a vector plot of the flowfield. After the velocity profiles had been developed, the shear stress at the wall was determined at each local x and y point using the one-seventh-power

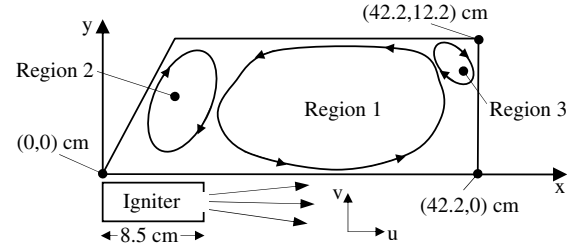


Fig. 4 Schematic of the igniter-induced flowfield structure with multiple recirculating flow fields.

law and the log law of wall (with $y^+ = 350$, the upper boundary of the log law of the wall [25]). Through the Reynolds analogy [26], the local Nusselt number could be determined using shear stress at the wall, local Reynolds number based upon the resultant velocity and the hydraulic diameter ($D_H = 2W$), and a Prandtl number. From this local Nusselt number, the local convective heat-transfer coefficient could be determined and used to find the convective heat-transfer rate at the wall at any given x and y point [Eqs. (4–7)]. Finally, the calculated heat-transfer rate for the recirculating flowfield was compared with the experimentally measured heat-flux rate and corrections were made to the velocity functions until matching heat fluxes were found:

$$\tau_w = 0.02187 \left(\frac{v}{WU_B} \right)^{\frac{1}{4}} \rho U_B^2 \quad (4)$$

$$\frac{C_f}{2} = \frac{\tau_w}{\rho U_B^2} = \frac{Nu_{D_H}}{Re_{D_H} Pr^{\frac{1}{3}}} \quad (5)$$

$$Nu_{D_H} \equiv \frac{h_c D_H}{k_f} \quad (6)$$

$$\dot{q}_{conv}'' = h_c (T_{gas} - T_{surf}) \quad (7)$$

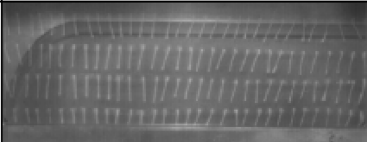

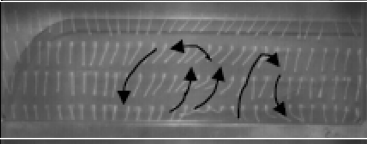
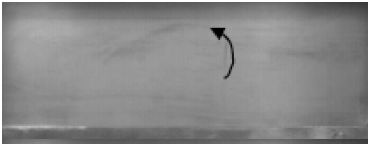
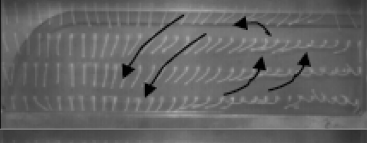
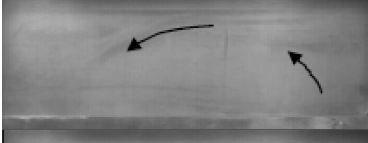
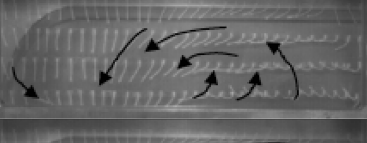
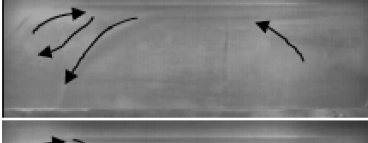
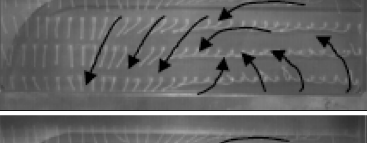

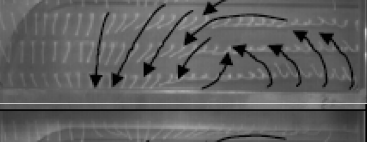

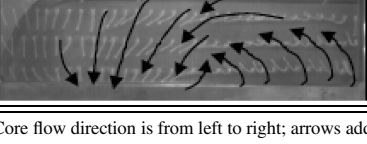
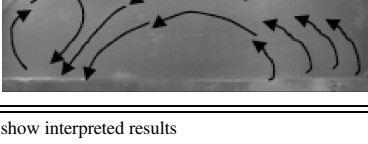
The radiation energy transfer rates at different locations in the fin-slot region have been found to be substantially smaller than the convective heat-transfer rates and, thus, neglected in this analysis. This was based upon calculations for four different cases of forced convection using igniter properties. These cases included forced convection for fully developed flow in a circular tube, gases in straight, smooth rectangular ducts (with and without well-rounded inlets), and gases in straight, smooth rectangular ducts using a correction factor for local h_c . Re_{D_H} was calculated using the bulk velocity, density of the igniter gas, and the hydraulic diameter, D_H . For all four forced convection cases, the resulting heat flux was found to be at least three times greater than that of the radiation heat flux.

V. Discussion and Results

Visualization tests with unheated air ($T_{BDT} = 298\text{ K}$) and CFD simulations were conducted with an \dot{m}_{ign} value around 0.159 kg/s. Multiple tests were conducted using both the chalk-powder/kerosene mixture and fine threads on the inner surface of the sacrificial windows. Selected frames from both the chalk-powder/kerosene mixture and fine thread on the sacrificial windows at the same time steps are shown in Table 1.

Based on the high-speed camera recordings of the flow in the fin-slot region, time variation of the flowfield pattern could be examined. Initially, the flow followed the geometry of the igniter nozzle, expanding at an angle of 27 deg until it impinged somewhere in the middle portion of the fin-slot region. The flow initially separated into two symmetric groupings of flow, each recirculating in opposite

Table 1 High-speed images of fine threads and chalk-powder covered window

Fine threads ^a	Chalk-powder kerosene	Time, ms	Comments
		Start	Start of testing; no flow observed
		293	Flow begins to enter the middle portion of the fin-slot region and tends to form two recirculation zones
		359	A large, counterclockwise circulation of flow develops in the middle portion of the fin as jet impingement point travels further downstream
		467	Counterclockwise recirculation zone becomes more prevalent downstream and a small recirculation zone develops near the surface
		589	Large recirculating loop gains momentum inducing a stronger surface region clockwise recirculating zone
		747	Flow is now in full circulation, inducing two eddies in the upper corners of the fin-slot region near the surface
		999	Few portions of chalk-powder kerosene remain, while the main recirculation in the fin-slot region still very strong

^aCore flow direction is from left to right; arrows added to show interpreted results

directions. As the flow velocity increased through the igniter nozzle, the flowfield eventually developed into a large group of counterclockwise recirculating loops of airflow, with only a small grouping of clockwise recirculating flow located in the upper, downstream section of the fin-slot region. According to the surface flow observation, there was also a small clockwise recirculating zone near the upper corner above the igniter exit. Further analysis of this trend can be explained from a typical photograph of the airflow pattern with fine threads, seen during quasi-steady operation, shown in Fig. 5.

The flow had reached a maximum velocity out of the igniter nozzle and induced a quasi-steady flow pattern with major amounts of flow entering into the fin-slot region from the downstream slot opening as opposed to the small amount of flow entering the middle section during the initial discharge period. This change can be explained by

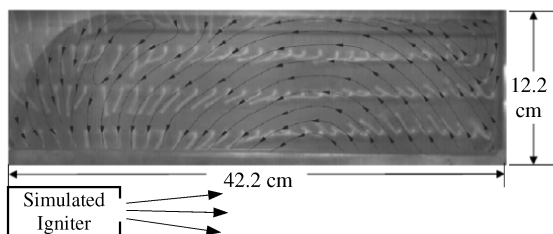


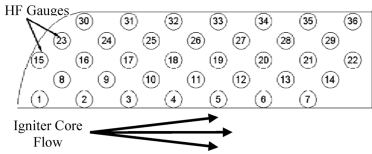

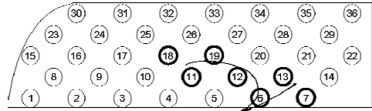

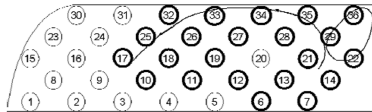
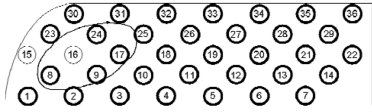

Fig. 5 Typical flow pattern of a head-end fin-slot region during quasi-steady operation.

the increase in Re_D and the rise in inertial forces of the core flow. At this moment, the flow pattern showed two nonsymmetric regimes: one large counterclockwise recirculation zone, which reentered the core flow, and some of which the flow recycled into the fin-slot region and the other flow regime was a small clockwise recirculation in the upper corner of the downstream section of the fin-slot region. The results of the cold-flow experiments showed good agreement with previous computational head-end fin-slot simulator motor burn sequence predictions [8], indicating that the flowfield of the hot burning gases through the igniter nozzle into the fin-slot region can have a strong influence on the overall heat-transfer and flame-spreading processes in the motor.

It was observed from the heat-flux data using live igniter firings that the initial igniter firing time period, from the triggering time at 0 ms to about 40 ms, experienced the most rapid dT/dt after the igniter discharge. Some gauges detected a change in temperature more quickly than others. This indicated that the flow of the igniter products through the fin-slot region has a highly nonuniform heating effect on the fin-slot sample at different locations. A representative time sequence of the live igniter flowfield is shown in Table 2.

The combustion products from the igniter, after exiting the igniter nozzle, expand radially outward until it impinged somewhere near the middle portion of the fin-slot region, around heat-flux gauges 6 and 7. The flow separated into two groupings, each recirculating in opposite directions. As the flow velocity increased through the igniter nozzle, the flowfield in the fin-slot region eventually turned into a large group of counterclockwise recirculating loops, with only a small grouping of clockwise recirculating flow located in the upper, downstream section of the fin-slot region. At this moment, the flow

Table 2 Time-sequenced flowfield patterns of the live igniter-induced flow

Flowfield pattern ^a	Time, ms	Comments
	Start	Start of testing; no flow observed
	13.5	Igniter product gas enters the fin-slot region at a location in the close vicinity of heat-flux gauges 6 and 7 in the first diagnostic row
	14.0	As the gas flow progresses upward through the fin slot, it starts to split into multiple flow fields, with one jet passing near gauge 13 and the other toward gauges 12, 19, 11, and 18
	15.0	Flow continued upward toward the top right corner of the fin-slot region passing near gauges 21, 14, 29, and 22, before splitting once again toward gauges 35, 28, 27, 26, and 18
	16.5	Gauges 36, 34, and 33 detected the rise in heat flux from the hot gas before the flow turned back toward gauges 22 and 26, 17, and 10, respectively
	18.0	The last field, near the head end, circulated weakly in the clockwise direction around gauges 17, 9, 8, 23, and 24
	200.0	At quasi-steady conditions, multiple recirculation zones inside of the fin-slot region

^aCore flow is from left to right; circled gauge positions and arrows show interpreted igniter flowfield results

pattern again showed two nonsymmetric regimes: a large counterclockwise recirculation zone, which reentered the igniter core flow, and small clockwise recirculation zones in the upper corners of the fin-slot region. These results agreed well with those observed from the flow visualization using cold air from the blow-down wind tunnel.

The results of the live igniter flow experiments also showed good agreement with previous computational head-end fin-slot simulator motor burn sequence predictions [8]. After the initial 40 ms, the flow pattern in the fin-slot region remained nearly unchanged for a relatively long period until 300 ms. Therefore, the major heat-transfer duration of the fin-slot propellant is dominated by the quasi-steady flowfield between 40 and 200 ms during the live igniter flow.

From this quasi-steady flowfield pattern, a functional form of the velocity profile with semi-empirical coefficients in the fin-slot region was developed. These velocity profiles were created by using the following procedure: 1) considering and constructing a flowfield structure in the open "rectangular" fin-slot region from a basic fluid mechanics point of view, 2) creating the velocity profiles by considering the igniter jet as the driving force for the recirculating flow, 3) applying no-slip conditions at the wall surfaces and introducing empirical constants based upon the recorded flowfield pattern, 4) employing the Reynolds analogy to link shear stress at the wall with the experimentally measured convective heat-transfer rate, and 5) considering the bulk flow in the fin-slot region is two

dimensional and independent of the z direction except in the region very close to the wall. By developing suitable functional forms of the u - and v -velocity components in the flowfield, one can assign a number of coefficients in the functional form to simulate the relative size of these recirculation zones. The mathematical functions can be regarded as semi-empirical, and the coefficients can be varied to account for different flow rates (change in density) and back pressures.

The equations for the u - and v -bulk velocity components are shown next. These equations can be used for regions 1–3 of Fig. 4, based upon x - and y -positions in the fin-slot region with H as the fin-slot region height and L as the fin-slot region length. By developing suitable functional forms of the u - and v -velocity components in the flowfield, one can assign a number of coefficients in the functional form to simulate the relative size of these recirculation zones.

Velocities for region 1: For $y/H \leq 0.655$

$$\lambda = 0.8L - \frac{y}{\tan \beta} \quad (8)$$

$$u_{\text{vel}} = u_{\text{max}} \sin\left(\frac{\pi y}{0.654H}\right) \times \left[1.29 \sin\left(\frac{\pi x}{\lambda} - \frac{\pi}{5} - \left(\frac{y}{\tan \beta} + 0.2L\right) \frac{\pi}{\lambda}\right) + 0.05 \right] \quad (9)$$

$$v_{\text{vel}} = -v_{\text{max}} \sin \left[\frac{2\pi x}{\lambda} - \left(\frac{y}{\tan \beta} + 0.2L \right) \frac{2\pi}{\lambda} \right] \times \left[0.05 \sin \left(\frac{y\pi}{H} \right) + 0.45 \right] \quad (10)$$

For $y/H > 0.655$

$$u_{\text{vel}} = -u_{\text{max}} \sin \left(\frac{\pi y}{0.346H} \right) \times \left[0.35 \sin \left(\frac{\pi x}{1.25\lambda} - \left(\frac{y}{\tan \beta} + 0.2L \right) \frac{\pi}{\lambda} \right) + 0.15 \right] \quad (11)$$

$$v_{\text{vel}} = -v_{\text{max}} \sin \left[\frac{2\pi x}{\lambda} - \left(\frac{y}{\tan \beta} + 0.2L \right) \frac{2\pi}{\lambda} \right] \times \left[0.35 \sin \left(\frac{y\pi}{H} \right) + 1.1 \right] \quad (12)$$

Velocities for region 2:

$$v_{\text{vel}} = v_{\text{max}} \sin \left[\frac{2\pi x}{0.4L} - \left(\frac{2\pi y \tan(\frac{\pi}{2} - \beta)}{0.2L} \right) + \frac{\pi}{8} \right] \times \left[0.001 \sin \left(\frac{2y\pi}{3H} \right) - 0.005 \right] \quad (13)$$

For $y/H \leq 0.655$

$$u_{\text{vel}} = -u_{\text{max}} \sin \left(\frac{\pi y}{1.308H} + \frac{\pi}{2} \right) [0.01655 \exp(x) - 0.0135] \quad (14)$$

For $y/H > 0.655$

$$u_{\text{vel}} = -u_{\text{max}} \sin \left(\frac{2\pi y}{0.346H} + \frac{\pi}{2} \right) [0.013 \exp(0.4x)] \quad (15)$$

Velocities for region 3: For $y/H \leq 0.655$

$$u_{\text{vel}} = 1.95u_{\text{max}} \sin \left(8 \frac{\pi y}{H} + \pi \right) \left[\sin \left(\frac{\pi x}{L} \right) + 0.45 \right] \quad (16)$$

$$v_{\text{vel}} = v_{\text{max}} \sin \left[\frac{8\pi x}{L} \right] \left[\sin \left(\frac{y\pi}{H} \right) + 0.61 \right] \quad (17)$$

Using the preceding equations, a flowfield was created. It is useful to note that the flowfield pattern, shown in Fig. 6, matches closely with the observed patterns from the windowed test rig shown in Tables 1 and 2. The largest vector in Fig. 6 represents a velocity magnitude of approximately 115 m/s.

To test the validity of the flowfield, the heat-transfer rate was calculated using the procedure described in Sec. IV.C.3. These results were then compared with the experimental values that were deduced from tests that were conducted using both hot airflow and live igniter-induced flow. Images of the event were captured by the high-speed camera from the start of the igniter trigger, as seen in Fig. 7.

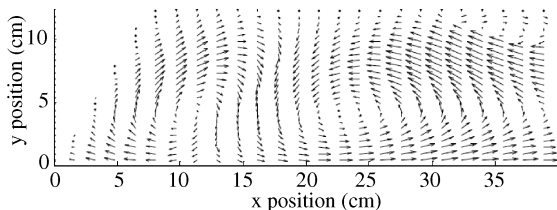


Fig. 6 Simulated flowfield in the fin-slot region based upon the bulk velocity components using the developed mathematical forms.

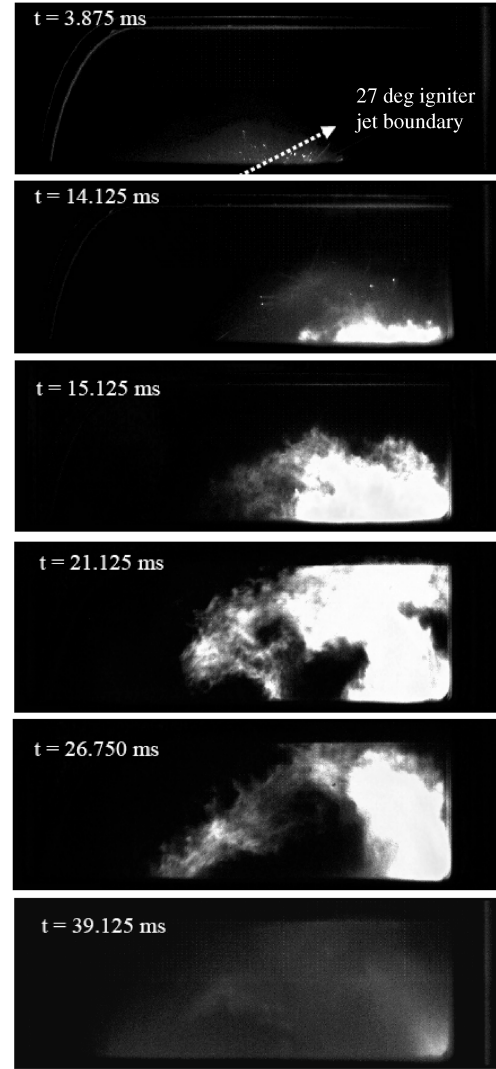


Fig. 7 A set of high-speed video images of the live igniter jet sequence in the fin-slot region at the filming rate of 10,000 pps over a 40 ms span (direction of igniter core flow is from left to right).

Using the mathematical expressions [Eqs. (9–17)] for the bulk velocity components, a heat-transfer correlation was developed to relate the local Nusselt number as a function of the local Reynolds number and Prandtl number as shown by Eq. (18):

$$Nu_{D_H} = 0.0261 (Re_{D_H, \text{local}})^{0.75} Pr^{1/3} \quad (18)$$

where

$$Re_{D_H, \text{local}} = \frac{\rho U_{\text{res}} D_H}{\mu} \quad (19)$$

The resultant velocity (U_{res}) is a function of a group of geometric parameters that include $\frac{x}{\lambda}$, $\frac{y}{H}$, $\frac{y}{\tan \beta}$, v , u_{max} , v_{max} , and $W_{\text{fin-slot}}$. The Nusselt number based upon the preceding correlation matched the calculated Nusselt number from the simulated flowfield within 10% and can therefore be used for heat-transfer rate calculations in the fin-slot region.

Measured heat-flux data were determined by using a fourth-order curve-fit on the temperature-time profiles at each heat-flux gauge position. Then, the dT/dt was entered in Eq. (1) to determine the heat-flux profile. The largest heat-flux corresponded to the highest slope in the initial temperature-rise region. The longer the test run, the greater the increase in temperature acting in the fin-slot region and the smaller the temperature difference, hence, a decrease in the heat-flux. The relative locations of the 36 heat-flux gauges on the diagnostic holder and row assignments can be seen in Fig. 8.

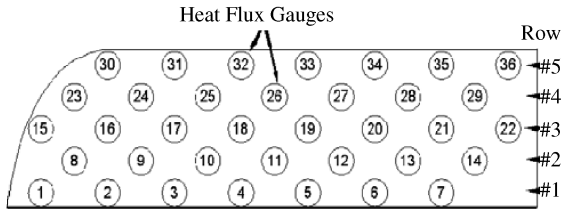


Fig. 8 Schematic diagram of the heat-flux gauge locations on diagnostic holder and row assignments.

In Figs. 9a–9e, the maximum calculated heat-flux values for a given row of gauges using the correlation shown in Eq. (18) were compared with measured maximum heat-flux values from the corresponding gauges. As shown in Figs. 9a–9e, the calculated maximum heat-flux distribution matched the measured data in a reasonable manner. Peaks in these heat-flux distributions indicate locations where the igniter-induced flowfield passed directly over the gauge locations and introduced a higher rate of energy transfer than the surrounding area. The plots showed that there are notable variations in the measured heat-transfer rates in the fin-slot locations from different igniter test runs. It was believed that these variations are partially due to the inconsistencies of the igniter propellant grains. In spite of these variations, the general trends of the heat-flux

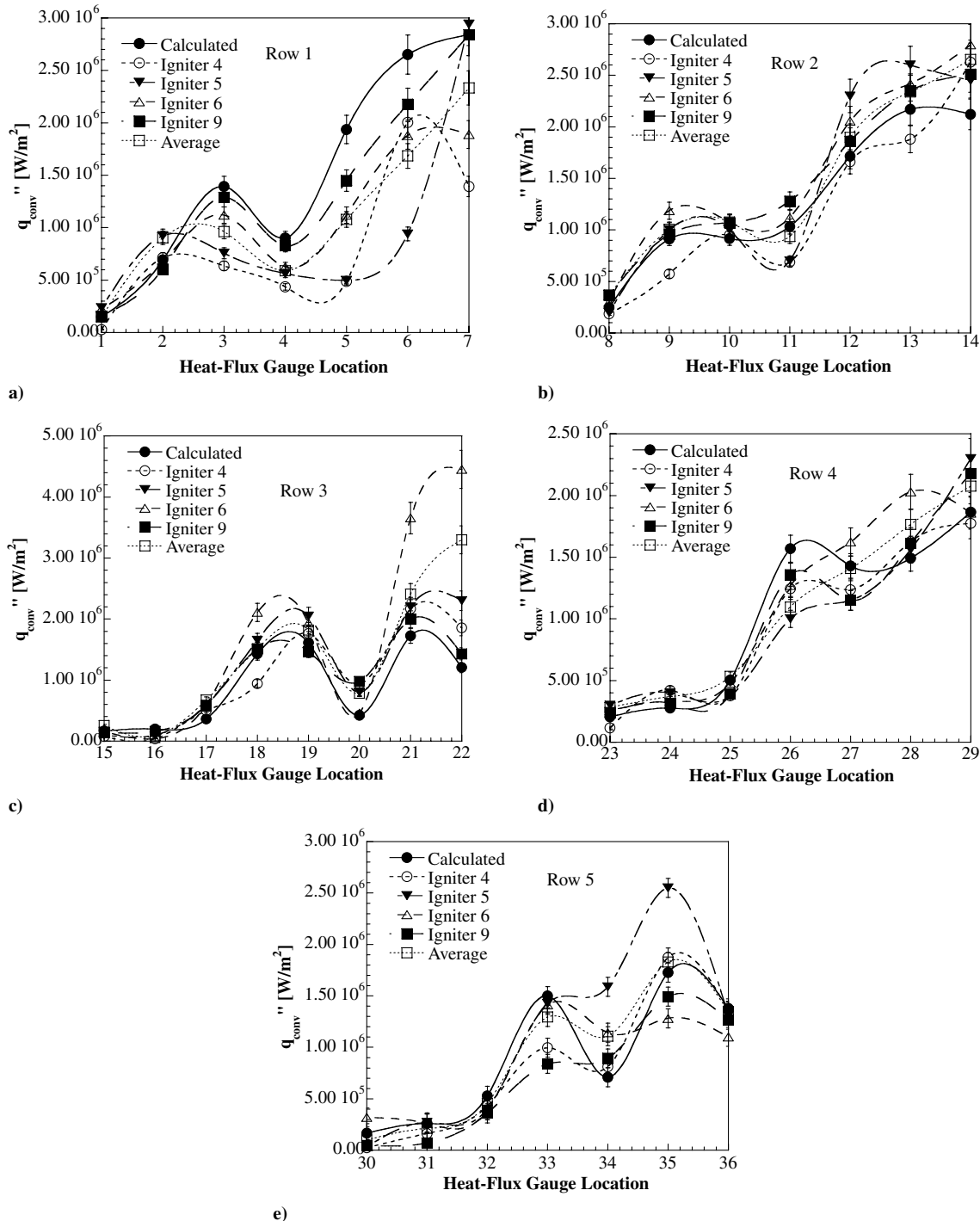


Fig. 9 Comparison of calculated maximum heat-flux distributions from developed empirical correlation with measured maximum heat-flux distributions from multiple live igniter tests in the fin-slot motor (plots a–e are based on heat-flux gauges in row number 1–5, respectively).

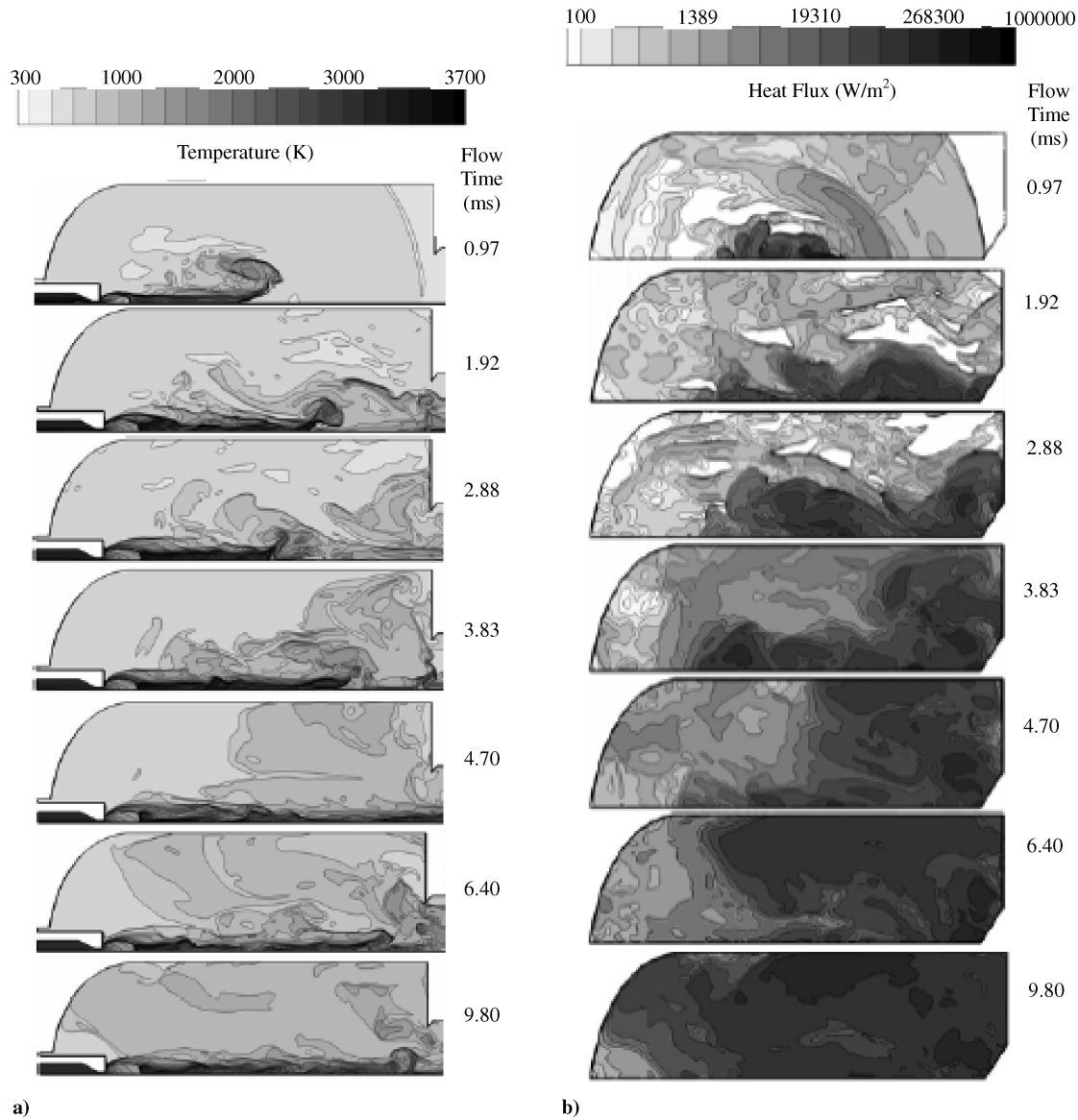


Fig. 10 Calculated a) gas temperature and b) heat-flux distributions during the early phase of the ignition event (direction of igniter core flow is from left to right and time is in milliseconds).

distributions showed certain degree of consistency at each row location.

The igniter-induced flowfield event using the CFD fin-slot grid and meshing scheme described in Sec. IV.C.2 was simulated for 10 ms. This computational time was a function of processor speed and meshing size and therefore was limited for this analysis. Care was taken to ensure that the value of y^+ is between 30 and 350 (i.e., in the log-wall region) on the propellant surface to ensure the validity of the wall functions. Note that $y^+ \equiv \rho u_t y / \mu$, where u_t is the friction velocity ($\equiv \sqrt{\tau_w / \rho}$). The results of the computational model are shown in Figs. 10a and 10b.

Calculated distributions of gas temperature and heat-flux on the surface of the inert propellant are shown in Figs. 10a and 10b, respectively. Driven by the discharge of the igniter jet, a portion of the initial vortex ring associated the expanding jet brings the hot igniter gases in contact with the propellant surface near the opening region of the fin slot. A counterclockwise recirculating-flow-induced heat transfer in the main region of the fin slot can be seen especially 9.80 ms from the start. Overall, the calculated progression of events compared very well with the heat-flux results shown in Table 2. The convectively dominated heat-transfer phenomena shown in these plots are matched with observed ignition and flame-spreading event described in Part II of this research work [15]. The CFD results given

previously were used to enhance our understanding of the heat-transfer rates and flowfield structure. In general, it gives the same trends as the experimentally observed flowfield structure and measured heat-flux distributions.

VI. Conclusions

An analysis of the flow pattern entering the fin-slot region of the head-end portion of an RSRM simulator is presented through cold- and hot-airflow experiments, CFD simulations, and live igniter flow with inert propellant. In total, over 30 cold/hot clean airflow experiments and 10 live igniters with inert fin-slot propellant tests were performed to observe the igniter-induced fin-slot flowfield and measure the heat-transfer at numerous locations along the propellant surface. The major findings from this fin-slot internal flowfield and heat-flux study include an improved understanding of the igniter-induced flowfield with several recirculating zones, the development of a heat-transfer correlation based upon detailed measurements of the highly nonuniform heat-flux distribution at various locations on the propellant surface. The detailed conclusions are described as follows:

- 1) During the transient portion of the cold-flow experiments, the airflow through the igniter nozzle impinged on the fin-slot region

somewhere near the middle section of the inert propellant, separating the flow into two counter-rotating recirculation zones. The major portion of the flow returned back toward the igniter, while the remaining flow exited the fin-slot region into the downstream center bore section.

2) This resulted in the formation of a large, recirculating flow over the entire length of the inert fin and two smaller and weaker recirculation zones above the igniter and in the upper downstream fin-slot region. The main recirculating flowfield dominated the heat-transfer characteristics in the fin-slot region as demonstrated by the measurement of heat fluxes from multiple locations. The CFD calculated results showed similar time variations of flow pattern as observed experimentally.

3) The flowfield reconstructed from the experiments matched closely with the quasi-steady recirculating flow pattern and was used in the development of a useful heat-transfer correlation for the fin-slot region. The heat-transfer rates evaluated from this correlation matched the measured data trend within the experimental error. This heat-transfer correlation can be used for future design and flame-spreading study of fin-slot motors with similar geometry to the existing RSRM.

4) The igniter-induced flowfield has a strong effect on the overall flame-spreading phenomena, essentially governing the forced convection energy transfer rates to the propellant surface.

Acknowledgments

The authors would like to acknowledge the support and encouragement of James Braithwaite of ATK-Launch Systems (the ATK Aerospace Launch Company) and Daryl Woods of NASA for this collaborative work conducted between Pennsylvania State University and ATK-Launch Systems through a contract funded via ARDEC at the office of Ray Pawlicki and Lee Harris. We would also like to thank Jonathan Janssen, Timothy Kibbey, Robert Lundgreen, Ounyoung Park, Brent Wiesenberg, and Mart Cook of ATK-Launch Systems for their input in our 1:10 RSRM simulator design, igniter propellant firing simulations, and propellant sample casting and shipment. In addition, we would like to thank Jerry Anderson and his Engineering Shop team at Pennsylvania State University for their excellent work in the manufacturing and modification of the laboratory-scale head-end fin-slot RSRM simulator.

References

- [1] Kumar, M., and Kuo, K. K., "Flame Spreading and Overall Ignition Transient," *Fundamentals of Solid Propellant Combustion*, edited by K. K. Kuo and Summerfield, Vol. 90, Progress in Astronautics and Aeronautics, AIAA, New York, 1984, pp. 305–360.
- [2] Most, W. J., Parker, K. H., and Summerfield, M., "The Ignition Transient in Solid Propellant Rocket Motors," *2nd AIAA/ASME/SAE/ASEE Joint Propulsion Conference and Exhibit*, AIAA Paper 1966-666, Colorado Springs, CO, 1966.
- [3] Mitchell, R. C., and Ryan, N. W., "Flame Spread on Solid Propellant," *Journal of Spacecraft and Rockets*, Vol. 2, No. 4, 1965, pp. 610–612. doi:10.2514/3.28243
- [4] Peretz, A., Kuo, K. K., Caveny, L. H., and Summerfield, M., "Starting Transient of Solid-Propellant Rocket Motors with High Internal Gas Velocities," *AIAA Journal*, Vol. 11, No. 12, 1973, pp. 1719–1727. doi:10.2514/3.50676
- [5] Johnston, W. A., "Solid Rocket Motor Internal Flow During Ignition," *Journal of Propulsion and Power*, Vol. 11, No. 3, 1995, pp. 489–496. doi:10.2514/3.23869
- [6] Chaouat, B., "Flow Analysis of a Solid Propellant Rocket Motor with Aft Fins," *Journal of Propulsion and Power*, Vol. 13, No. 2, 1997, pp. 194–196. doi:10.2514/2.5169
- [7] Kuo, K. K., Kokal, R. A., Paulauskas, M., and Alaksin, P., "Flame-Spreading Phenomena in Fin Slots of a Solid Rocket Motor," *Journal of Propulsion and Power*, Vol. 17, No. 5, 2001, pp. 1005–1011. doi:10.2514/2.5862
- [8] Ciucci, A., Jenkins, R. M., and Foster, W. A., Jr., "Analysis of Ignition and Flame Spreading in Solid Rocket Motor Star Slots," *Journal of Propulsion and Power*, Vol. 11, No. 6, 1995, pp. 1371–1373. doi:10.2514/3.51447
- [9] Sutton, G. P., and Biblarz, O., *Rocket Propulsion Elements*, 7th ed., Wiley, New York, 2001, pp. 48–96 and 544–545.
- [10] Timmat, Y. M., *Advanced Chemical Rocket Propulsion*, Academic Press, New York, 1987, pp. 197–214.
- [11] Gatland, K., *Space Technology*, Salamander Books, Ltd., New York, 1981, pp. 198–213.
- [12] Caveny, L. H., Kuo, K. K., and Shackelford, B. W., "Thrust and Ignition Transients of the Space Shuttle Solid Rocket Motor," *Journal of Spacecraft and Rockets*, Vol. 17, No. 6, 1980, pp. 489–494. doi:10.2514/3.28041
- [13] Parker, K. H., Wenograd, J., and Summerfield, M., "The Ignition Transient in Solid Propellant Rocket Motors," *Solid Propellant Rocket Conference*, AIAA Paper 1964-126, Palo Alto, CA, 1964.
- [14] Bai, S. D., Han, S. S., and Pardue, B. A., "2-D Axisymmetric Analysis of SRM Ignition Transient," *29th AIAA/ASME/SAE/ASEE Joint Propulsion Conference and Exhibit*, AIAA Paper 1993-2311, Monterey, CA, 1993.
- [15] Moore, J. D., Kuo, K. K., and Ferrara, P. J., "Flame-Spreading Behavior in a Fin-Slot Solid Propellant Rocket Motor Grain (Part II)," *Journal of Propulsion and Power* (to be published).
- [16] McAlevy, R. F., III, Magee, R. S., Wrubel, J. A., and Horowitz, F. A., "Flame Spreading over the Surface of Igniting Solid Rocket Propellants and Propellant Ingredients," *AIAA Journal*, Vol. 5, No. 2, 1967, pp. 265–271. doi:10.2514/3.3951
- [17] Kulkarni, A. K., Kumar, M., and Kuo, K. K., "Review of Solid-Propellant Ignition Studies," *16th AIAA/ASME/SAE/ASEE Joint Propulsion Conference and Exhibit*, AIAA Paper 1980-1210, Hartford, CT, 1980.
- [18] Moore, J. D., Ferrara, P. J., Wehrman, R. B., and Kuo, K. K., "Internal Flow Field Structure in a Simulated Fin-Slot Rocket Motor," *41st AIAA/ASME/SAE/ASEE Joint Propulsion Conference and Exhibit*, AIAA Paper 2005-3955, Tucson, AZ, 2005.
- [19] Kuo, K. K., *Principles of Combustion*, 2nd ed., Wiley, New York, 2005, pp. 18 and 655.
- [20] John, J. E. A., *Gas Dynamics*, 2nd ed., Prentice-Hall, Upper Saddle River, NJ, 1984, p. 46.
- [21] Shur, M., Spalart, P. R., Strelets, M., and Travin, A., "Detached-Eddy Simulation of an Airfoil at High Angle of Attack," *Engineering Turbulence Modelling and Experiments 4: Proceedings of the 4th International Symposium on Engineering Turbulence Modelling and Measurements*, 1999, pp. 669–678.
- [22] Spalart, P., and Allmaras, S., "A One-Equation Turbulence Model for Aerodynamic Flows," AIAA Paper 92-0439, 1992.
- [23] Liou, M. S., and Steen, C. J., Jr., "A New Flux Splitting Scheme," *Journal of Computational Physics*, Vol. 107, No. 1, 1993, pp. 23–39. doi:10.1006/jcph.1993.1122
- [24] Liou, M. S., "A Sequel to AUSM: AUSM+," *Journal of Computational Physics*, Vol. 129, No. 2, 1996, pp. 364–382. doi:10.1006/jcph.1996.0256
- [25] Munson, B. R., Young, D. F., and Okiishi, T. H., *Fundamentals of Fluid Mechanics*, 3rd ed., Wiley, New York, 1998, p. 484.
- [26] Incropera, F. P., and DeWitt, D. P., *Fundamentals of Heat and Mass Transfer*, 5th ed., Wiley, New York, 2002, p. 363.

K. Frendi
Associate Editor